ELSEVIER

Contents lists available at ScienceDirect

Surface & Coatings Technology

journal homepage: www.elsevier.com/locate/surfcoat





In-situ NbC reinforced Fe-based coating by laser cladding: Simulation and experiment

Liaoyuan Chen, Tianbiao Yu^{*}, Pengfei Xu, Bo Zhang

School of Mechanical Engineering and Automation, Northeastern University, Shenyang, China Liaoning Provincial Key Laboratory of High-end Equipment Intelligent Design and Manufacturing Technology, Shenyang, 110819, China

ARTICLE INFO

Keywords:
Laser cladding
Finite element model
Composite coating
In-situ reaction
Solidification characteristics
Mechanical properties

ABSTRACT

In-situ NbC reinforced Fe-based coating was fabricated on the middle carbon steel surface by laser cladding with the mixture of niobium and boron carbide powder, aiming at revealing the mechanism of in-situ synthesis and improving the hardness and wear performance. The possibility and mechanism of in-situ synthesis were explored for the first time by combining simulation with experiment. The phase composition, microstructure characteristics and evolution mechanisms of the coatings were investigated by X-ray diffraction and scanning electron microscopy. The strengthening mechanism of hard phases on hardness and wear performance of coating were analyzed in detail. The results show that Marangoni convection promoted the melting of particles and improved the uniformity of solute atoms. The composite coating is mainly comprised of reinforced phases (NbC, Fe₂B, B₄C) and the matrix ([Fe—Cr] solid solution). The dispersive NbC particles (average diameter $\sim 1.03~\mu m$) in-situ formed at the grain boundary achieved the dispersion and fine-grained strengthening effect. The hardness of the composite coating is 866.36 HV_{0.5}, which is 3.95 times and 4.16 times that of the substrate and Fe-based coatings. The volume loss of composite coating reduced more than five times as compared to the substrate and Fe-based coating, and the wear mechanism changed from abrasive wear to adhesive wear due to the addition of Nb and B₄C powders.

1. Introduction

Laser-clad metal matrix composite (MMC) coating has been widely used in surface modification or remanufacturing of turbine blades, rolls, gears, shafts and guide rails due to its high bonding strength and hardness, small heat-affected zone, good wear resistance, corrosion resistance and wide material applicability [1–3]. It usually consists of matrix phases including Fe, Ni, Co, Ti and so on and the strengthen phases including ceramics, intermetallic compounds and so on [4,5]. Since ceramics exhibit good chemical stability, high hardness and wear resistance, they are widely used as candidates to improve the surface properties of materials [6,7]. Up to now, the reinforced ceramic phases in laser cladding composite coating are mainly produced by direct addition or in-situ synthesis.

In recent years, the reinforced ceramics particles such as WC [8], NbC [9], SiC [10], and TiC [11] have been directly added to the coating material, and the hardness and wear resistance of the coating are indeed improved. However, the researchers also have found that the toughness and crack resistance of the coating would be reduced due to the great

differences of elastic modulus, expansion coefficient and lattice properties between ceramics and matrix. Moreover, since laser cladding process has the characteristics of rapid melting and non-equilibrium solidification, the shape and chemical composition of the directly added ceramics particles are difficult to ensure chemical stability.

To overcome the above limitations, the in-situ ceramic particles reinforced composite coating prepared by laser cladding have received more attention. Gui et al. [12] prepared in-situ TiC reinforced Ni-based coating on grey cast iron by laser cladding. The Rockwell hardness and wear loss of the coating prepared with 20 wt% Ti—C precursors are 1.88 and 0.22 times of that of the substrate, respectively. Zeng et al. [13] had preset uniformly mixture with pure titanium (50 wt%), boron nitride (33.8 wt%) and graphite (16.2 wt%) powder on the surface of Ti-6Al-4V alloy, followed by laser melting. The reinforcements in the layer were mainly composed of Ti(C, N) phases with dendritic size and fine-structure TiB phases. The hardness of Ti-6Al-4V was increased 180 HV, and the wear volume loss of the composite layer was half that of the substrate after 8 h wear time. In order to improve the low hardness and poor wear-resistance of 316L stainless steel, AlMangour et al. [14]

^{*} Corresponding author at: School of Mechanical Engineering and Automation, Northeastern University, Shenyang, 110819, China. *E-mail address:* tianbiaoyudyx@gmail.com (T. Yu).

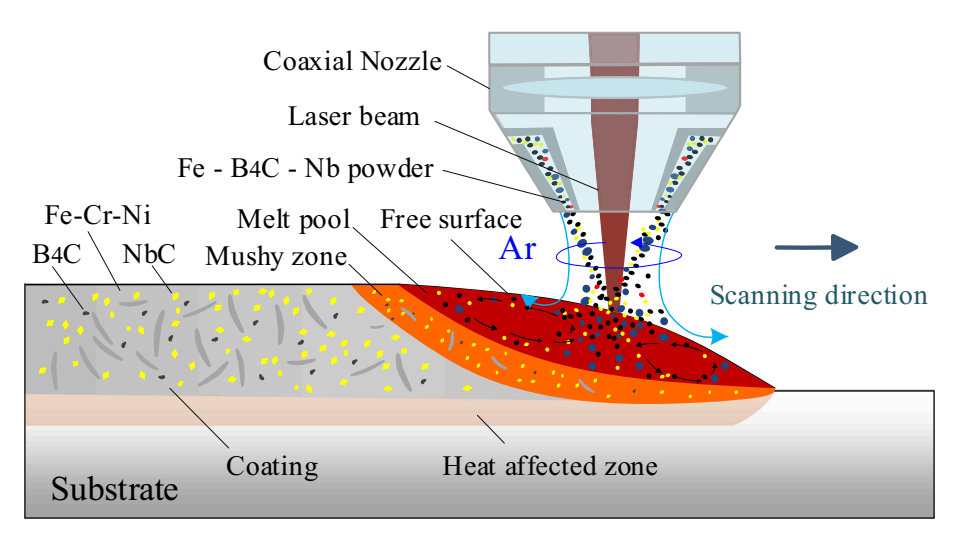


Fig. 1. The principle of in-situ ceramic particles by laser cladding.

explored the effect of laser volume energy on the densification, microstructure, hardness and wear properties of the in-situ TiC reinforced coating. Results show that TiC phase could be completely formed only when energy densities was higher than 67 J/mm³, the volumetric energy densities of 300 J/mm³ and 100 J/mm³ corresponded to optimum densification of 98.88% and lowest wear rate of $1.31 \times 10^{-4} \text{mm}^{\bar{3}} / N \cdot \text{m}$, respectively. Tijo et al. [15] successfully prepared in-situ TiC-TiB2 coating on titanium alloy surface by tungsten inert gas cladding process, and analyzed the effect of process parameters on the microstructure evolution in detail. The analysis showed that the relative percentage of ceramic phases decreased with the increase of scanning speed, but increased with the increase of current. Since the reinforcements which in-situ synthesized are steady in chemically and thermally, fine and uniform in size, and good bonding with matrix in the works of literature review, this behavior ensures that the composite coating has sufficient strength to carry large loads [16,17]. However, the numerous works in the experiments and theoretical analysis also show that the requirements of the temperature evolution for the in-situ reaction is very harsh [18,19]. Moreover, laser cladding is a non-equilibrium metallurgical process, and the melting and cooling rate are more than 10⁶ K/s [20,21]. The mechanism of in-situ synthesis is an important and practical problem in the laser cladding process of rapid melting and solidification. To date, it is not mature to study the growth mechanism of reinforcement phases in the coating by the experimental method, which increases the difficulty of in-situ ceramic particles reinforced coating by laser cladding. Therefore, a simulation model of laser cladding for preparing MMC coating s is of great significance for analyzing the mechanism of in-situ reaction, the growth process of the ceramic particles, the phase composition, and the optimization of the process.

According to literature studies [7,9,22], the NbC ceramics have high hardness and melting point, low friction coefficient, and ideal wettability with Fe-based alloys. Therefore, the boron nitride (B₄C) and niobium (Nb) powders were added to the Fe-based powder, and it was desired to in-situ NbC particles in the composite coating by laser cladding in this study. The possibility and mechanism of in-situ reaction were explored for the first time by combining simulation with experiment during laser cladding process. The effect of heat and mass transfer on migration and melting behavior of particles was explored in detail. Moreover, phases and microstructure were investigated systematically according to thermodynamic calculation and simulated thermal parameters. Finally, the mechanism of in-situ NbC particles on improving the hardness and wear performance was emphatically revealed. This study focuses on providing a theoretical reference for laser-clad in-situ ceramic composite coating, which will be beneficial for improving the properties of laser-clad MMC coating.

2. Numerical modeling

Fig. 1 shows the principle of in-situ NbC ceramic particles by laser cladding. The following assumptions and simplifications are proposed for the model: $\frac{1}{2}$

- The liquid in the molten pool is a laminar, viscous, and incompressible Newtonian fluid.
- 2. The materials of the composite powder and the substrate are isotropic, and the internal components are evenly distributed.
- Only the powder entering the molten pool contributes to the growth of the deposition track.
- 4. Material evaporation is not considered in the model.

2.1. Governing equation

The multiple liquid phases (MLPs) in the molten pool could be considered an incompressible fluid governed by the Navier-Stokes and continuity equation as follows,

$$\rho \frac{\partial \mathbf{u}}{\partial t} + \rho(\mathbf{u} \cdot \nabla \mathbf{u}) = -\nabla(\mathbf{p} \cdot \mathbf{I}) + \nabla \left[\mathbf{u} \cdot \left(\nabla \mathbf{u} + (\nabla \mathbf{u})^{\mathrm{T}} \right) \right] + \rho \mathbf{g} \beta (T - T_0) - K_0 \frac{(1 - f_l)^2}{f_l^3 + B} \mathbf{u}$$
(1)

$$\frac{\partial \rho}{\partial t} + \rho \nabla \cdot (\mathbf{u}) = 0 \tag{2}$$

in which ρ is the density, u is the velocity, t is time, u and p are dynamic viscosity and pressure, respectively of the fluid, and \mathbf{g} is the vector of gravitational acceleration. The third term on the right side of Eq. (1) represents the Buoyancy force, in which β is the thermal expansion coefficient, T and T_0 are the temperatures and initial temperature of the material. The last term on the right side of Eq. (1) represents momentum dissipation in the mushy zone, in which K_0 is a constant that depends on the morphology of the porous media (2 × 10⁷ in this study), B is a small constant (10⁻³in this study), B is liquid mass fraction defined as follow.

$$f_{l} = \begin{cases} S\left(\frac{T - T_{s}}{T_{l} - T_{s}}\right) & T < T_{s} \\ S\left(\frac{T - T_{s}}{T_{l} - T_{s}}\right) & T_{s} \le x \le T_{l} \\ 1 & T_{l} \end{cases}$$

$$(3)$$

where S(x) is a step function, T_s and T_l are the liquidus and solidus of the substrate, respectively.

The heat transfer equation in the model is defined by Eq. (4).

$$\rho C_p \frac{\partial T}{\partial t} + \rho C_p \mathbf{u} \cdot \nabla H = \nabla (k \nabla T) - \frac{\partial H}{\partial t} - \rho \mathbf{u} \cdot \nabla H$$
(4)

in which, k is the thermal conductivity, H is the latent enthalpy content of fusion, which is given as $\Delta H = L \cdot f_l$. L is the latent heat of the phase change of the material from solid to liquid.

2.2. Boundary conditions

The distribution of laser heat flux (I_0) on the free surface was set as Gaussian, which can be defined as follow,

$$I_{0} = \frac{2P\eta_{l}}{\pi \cdot r_{L}^{2}} exp\left(\frac{-2\left(\left(x - Vs \cdot t\right)^{2} + y^{2}\right)}{r_{L}^{2}}\right) - h_{c}(T - T_{0}) - \sigma_{b}\varepsilon\left(T^{4} - T_{0}^{4}\right)$$
 (5)

where P and r_L are laser power and laser beam radius, respectively, x and y are the distances to the laser beam on the free surface, Vs is scanning speed, h_c , σ_b and ε are the heat transfer coefficient, Stefan-Boltzmann constant and the emissivity, respectively. η_l is the absorption efficiency of laser energy to the composite powder and can be calculated as,

$$\eta_l = \sum \alpha_i A_i \tag{6}$$

where α_i is the volume fraction of the *i*th phase and A_i is the laser absorption of the *i*th phase, which is computed via Hagen–Rubens relationship, and can be defined by [23].

$$\mathbf{A}_{i} = 0.1457 \sqrt{\rho_{s}/\lambda} + 0.09 exp\left(-0.5 \sqrt{(\lambda - c/N)/\rho_{s}}\right) \tag{7}$$

where ρ_s is the resistivity, N is the number of extranuclear electron layers of material atoms, λ is the laser wavelength, and c is a constant (2.1 \times 10⁻⁶).

The momentum boundary at the free surface interface incorporating the capillary force and thermocapillary force is defined as,

$$F = \sigma \kappa \mathbf{n} + \frac{\partial \sigma}{\partial T} \left[-\mathbf{n} (\mathbf{n} \overrightarrow{\nabla}_s T) \right]$$
 (8)

where σ is surface tension, κ and n are the normal and curvature of the free surface, respectively.

The free surface moving speed $(V_{L/G})$ is mainly related to the mass addition and the liquid flow in the molten pool, and can be defined as,

$$V_{L/G} = V_p \cdot \mathbf{n} + \mathbf{u} \cdot \mathbf{n} \tag{9}$$

where u is the velocity of the liquid metal on the free surface, V_p is the moving velocity of the free surface due to mass addition. The calculation of V_p is given by,

$$V_{p} = \frac{2V_{f} \cdot \eta_{m}}{\pi \cdot \rho_{m} r_{p}^{2}} exp\left(\frac{-2\left(\left(x - Vs \cdot t\right)^{2} + y^{2}\right)}{r_{p}^{2}}\right) \cdot S\left(\frac{T - T_{s}}{T_{l} - T_{s}}\right)$$
(10)

where V_f is powder feed rate, η_m is powder catchment efficiency, ρ_m is the density of composite powder, r_p is the powder flow radius, which was obtained by calibrating the image collected by the high-speed camera. The last term of Eq. (8) shows that only composite powders that exceed their solidus can contribute to the growth of the coating.

2.3. Numerical solution

The heat and mass transfer of the 3D finite element established in this paper are shown in Fig. 2. The solution domain size of the model is $8\times6\times4$ mm³. The boundary layer theory was used to refine the grids of the key fluid region. The number of grids in this region is 0.168 mm and the minimum size is 0.9 mm. A time-dependent solver with a maximum step size of 0.05 s was employed.

The thermal and physical properties of the Fe-based powder, substrate, B_4C and Nb are listed in Table 1. Since the substrate and the

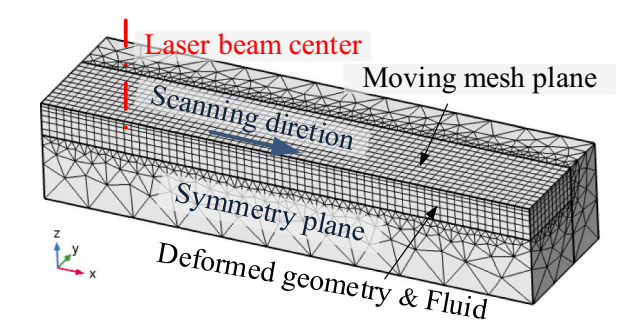


Fig. 2. Schematic diagram of numerical domains.

Table 1 Physical properties of the substrate, Fe-based powder, B₄C and Nb particles.

Property	Substrate	Fe-based powder	B ₄ C	Nb
Solidus temperature (K)	1680	1495	_	-
Liquidus temperature (K)	1757	1708	2623	2741
Gasification temperature (K)	3000	3090	3773	5015
Solid density (kg m ⁻³)	7077	7850	2.52	26.4
Liquid density (kg m ⁻³)	5880	6130	2.52	26.4
Specific heat capacity (J/(kg·K))	830	755	24.61	260
Thermal conductivity (W/(m·K))	33.85	46.33	_	53.7
Latent heat of fusion (kJ kg ⁻¹ K ⁻¹)	247.18	270	_	26.4
Coefficient of thermal expansion $(10^{-5}/K)$	1.05	1.3	-	-
Surface tension coefficient (N/m)	1.77	1.76	_	_
Change rate of surface tension	$-4.18 \times$	$-4.002 \times$	_	_
coefficient with temperature (N/ (m·K))	10^{-4}	10^{-4}		
Dynamic viscosity (Pa·s)	$\begin{array}{c} 1.92 \times \\ 10^{-3} \end{array}$	$\begin{array}{c} 2.25 \times \\ 10^{-3} \end{array}$	-	-

composite powder were fully mixed in the molten pool, the material properties of the solution (such as thermal conductivity, specific heat capacity, and dynamic viscosity) were assumed to be linearly dependent on the material properties of the substrate and the composite powder. The initial thermal physical parameter (M_0) in the molten pool is based on the initial plane Z_0 , which could be defined by

$$M_0 = S\left(\frac{z_0 + \Delta z - z}{\Delta z}\right) \cdot M_p + S\left(\frac{z - z_0 - \Delta z}{\Delta z}\right) \cdot M_s$$
 (11)

where M_p and M_s are the material properties of the metal powder and the substrate, respectively, Z_0 is the initial plane, S(x) is a step function, Δz (8 · $10^{-6}m$) is a sufficiently small constant associated with the coating height. The process parameters for calculations and experiment are shown in Table 2. The powder catchment efficiency was measured by the mass change of the substrate before and after cladding.

 Table 2

 The processing parameters for calculations and experiments.

Parameter	Value & units
Power P	350 W
Beam diameter (r_L)	1.0 mm
Scan speed (V _s)	5.5 mm/s
Powder feed rate (V_f)	7.72 g/min
Powder catchment efficiency (η_m)	0.26
Laser absorption ratio (η _l)	0.3
Convective heat transfer coefficient (h _c)	$100~{\rm Wm^{-2}~K^{-1}}$
Emissivity (ε_0)	0.36
Boltzmann constant (σ_b)	$1.38 \times 10^{-23} \text{ J/K}$
Ambient temperature (T_0)	300 K
Shielding gas	Ar

Table 3Chemical compositions of the Fe-based powder and substrate (wt%).

Element	С	Cr	Si	Ni	В	Mn	Cu	P	Fe
Fe-based powder	0.1-0.2	14–18	1.0-1.5	2.0-2.5	1.0-2.0	0.2-0.5	_	_	Bal.
Substrate	0.42-0.50	\leq 0.2	0.17 - 0.37	≤0.30	_	0.50-0.80	≤0.25	≤0.035	Bal.

3. Materials and experimental procedures

The experimental equipment used in this study is a coaxial laser cladding system [24]. The substrate material (size $100 \times 100 \times 10 \text{ mm}^3$) is middle carbon steel. Table 3 presents the chemical compositions of the Fe-based powder and substrate. The deposition material of the coating alloy was prepared from Fe-based powder (80 wt%, average particle size \sim 103.76 µm), B₄C powder (purity >99.5%, 10 wt%, average particle size $\sim 80.30 \ \mu m)$ and Nb powder (purity > 99.5%, 10 wt%, average particle size $\sim 80.88 \mu m$). The scanning electron microscopy (SEM) images and size statistics of the Fe-based, B₄C, and Nb powders are shown in Fig. 3. The optimized mass ratio of Nb and B₄C powder not only does not reduce the fluidity of the composite powder but also can ensure the volume fraction of in-situ NbC phases in the composite coating and further improve the properties. Besides, the atomic ratio of C to Nb is about 3:2, which ensures that enough C atom can react with Nb atom to form NbC when the oxidation of B₄C is considered. The composite powder was mixed for 3 h using a planet-type ball mill with a rotation speed of 400 rpm. The milling media (stainless steel balls) to powder ratio was fixed at 2:1. The powder was dried at 100 °C for 2 h in a constant temperature drying oven. Before experiments, the upper surface of the substrate was polished with 600-grit SiC abrasive papers and cleaned with alcohol to remove the dirt.

After the experiment, the test samples of $20~\text{mm} \times 10~\text{mm} \times 10~\text{mm}$ were cut from the substrate along perpendicular the scanning direction by a wire cutting machine. For microstructural observations, the cross-section of the sample was grounded from 240 to 2000 grit SiC abrasive papers, mechanically polished to a mirror finish, and then corroded for 15 s by the aqua regia (hydrofluoric acid: nitric acid = 3:1, vol%). The cross-sectional morphology, microstructure, and phases of the coatings were investigated by SEM (Zeiss, Germany) equipped with

energy dispersive spectroscopy (EDS). The phases in the powders and coatings were investigated by an X-ray diffractometer (XRD, X Pertpro, Netherlands). A scanning range from 10 to 90 degrees was employed at the scanning rate of 8 degrees/min with measurement accuracy, $\pm 0.01^{\circ}$. The hardness of the cross-section of coatings was evaluated on polished and corroded planes by Vickers hardness indenter (HV-1000, Shanghai Hengyi Precision Instrument Co., Ltd., Shanghai, China), with a load of 500gf and a load-dwell time of 15 s along the growth direction. Three hardness tests were carried out for each hardness sample to avoid the error. The dry sliding test was performed on the multifunctional material surface property tester (MFT-4000, Lanzhou Institute of physical chemistry, Chinese Academy of Sciences, Lanzhou, China) to analyze the tribological properties of the coatings with normal loading:10 N, reciprocating distance: 5 mm, sliding speed: 220 mm/min, sliding time: 40 min, temperature: 25 \pm 1 $^{\circ}\text{C}.$ The material of the friction pair was zirconia (hardness: HRC > 90) with a diameter of 5 mm. The friction coefficient of samples was recorded by a computer during the sliding test. Prior to the sliding tests, the surface of samples was mechanically polished and then ultrasonically cleaned for 5 min in acetone to remove the surface dirt. The error factors caused by porosity, cracks, and inhomogeneity of microstructure had been avoided as far as possible before the sliding test. The 2D (two dimensional) and 3D morphology of worn surfaces were observed by the laser confocal microscope (OLS4000, Japan). Fig. 4 shows the 2D profile schematic diagram of the wear track. The wear volume (V_{Loss}) could be calculated by Eq. (12),

$$\mathbf{V}_{Loss} = L \cdot \left[(x_2 - x_{1x}) \cdot y_1 - \int_{x_1}^{x_2} S_{(x)} dx \right]$$
 (12)

where L is the reciprocating distance, $S_{(x)}$ is a 2D profile of wear track, which was measured by the laser confocal microscope. Since the wear

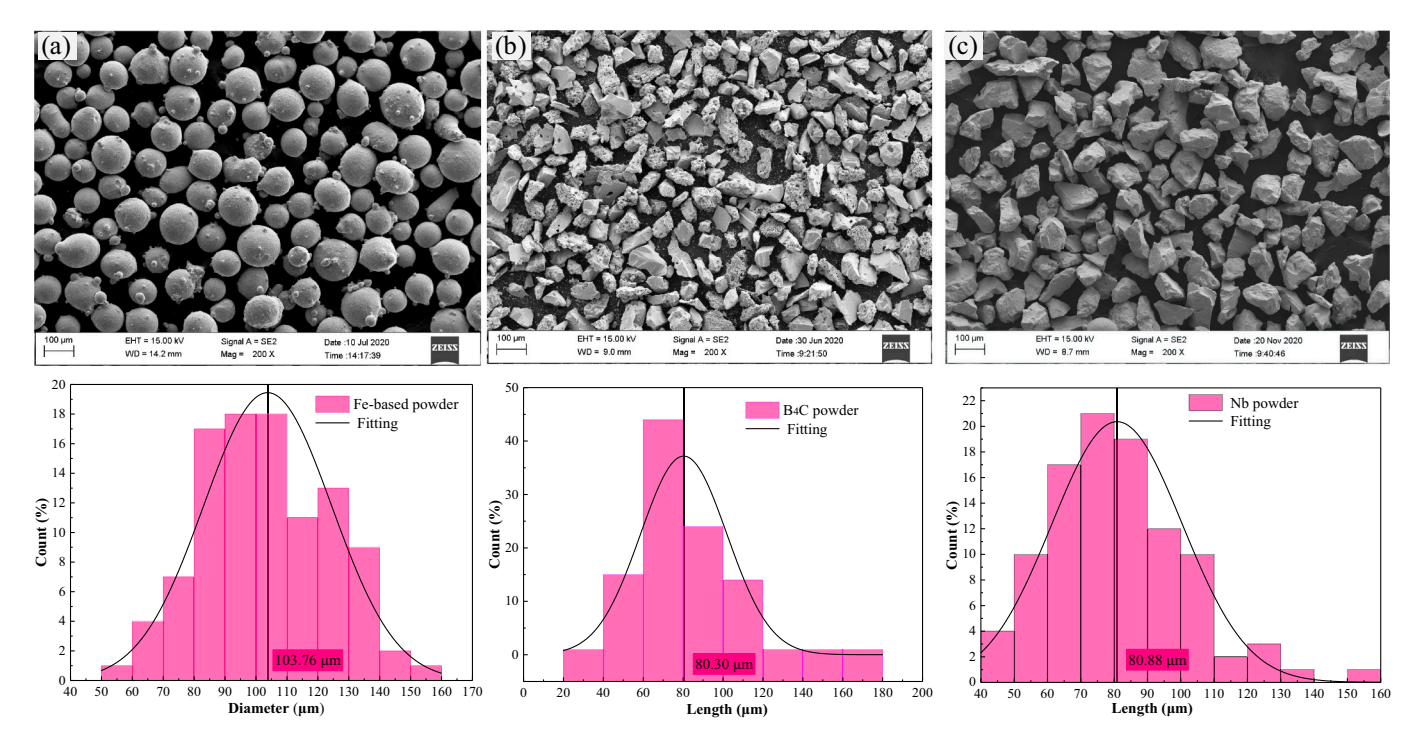


Fig. 3. SEM image and size statistics of (a) Fe-based powder, (b) B₄C powder, and (c) Nb powder.

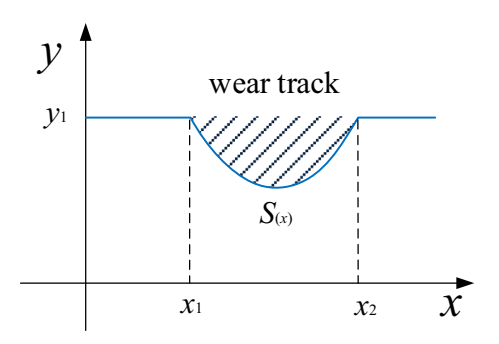


Fig. 4. The 2D profile schematic diagram of wear track.

volume is far less than the weight of the test sample, the error of wear volume could be greatly reduced due to its powerful data processing ability and high measurement accuracy (horizontal resolution: $0.12~\mu m$, vertical resolution: $0.01~\mu m$).

4. Results and discussion

4.1. Heat and mass transfer

Fig. 5 shows the temperature evolution of the molten pool. The very smooth coating surface indicates that the computed accuracy of the model is high. In the initial laser cladding, the temperature of the molten pool raised rapidly due to the high laser energy density. At the time of 100 ms, the maximum temperature exceeded the liquidus of the molten pool, so the composite coating began to grow, as shown in Fig. 5(a). After about 300 ms later, the maximum temperature of the molten pool exceeded 2800 K, so the B₄C and Nb particles began to melt. By comparing Fig. 5(c) and (d), it can be found that the temperature, velocity magnitude, and shape of the molten pool tend to stabilize after about 500 ms. Since the maximum temperature in the quasi-steady molten pool exceeds the liquidus of all powders, this provides the basic criterion for the in-situ synthesized NbC particles in the solidified coating.

Since the Marangoni convection in the molten pool is so strong (maximum velocity over 100 mm/s), the metal liquid will be recycled many times before solidification [25,26]. This phenomenon significantly causes the redistribution of elements and promotes the dissolution of high-melting particles, and further affects the solidified

microstructure which is governed by thermal parameters and solute concentration during solidification [27]. Fig. 5d also that the zone beyond the B_4C and Nb liquidus is very small. This phenomenon results in a large number of B_4C and Nb powders cannot melt fully when entering the molten pool. Therefore, it is meaningful to evaluate the convection recycling times of liquid metal and its effect on solute concentration.

To evaluate the conversion recycling times, the computed flow velocity, molten pool size, and liquid lifetime were extracted. Fig. 6 shows the superimposed temperature and velocity fields of the quasi-steady molten pool. As shown in Fig. 6(a), the metal flow is counterclockwise at the end of the molten pool. This behavior causes the high-temperature liquid at the center of the molten pool to flow to the end and improves the uniformity of temperature distribution (Fig. 6b). Fig. 6(b) also shows that the velocity magnitude on the surface of the molten pool is positively correlated with G. The maximum velocity on the surface of the molten pool is more than 120 mm/s, and the average velocity is 71.04 mm/s. As shown in Fig. 6(c), the size of the quasi-steady molten pool is approximately an ellipse with 1.950 mm in the length of the long axis (L_I) and 1.210 mm in the length of the short axis (L_S) . The perimeter (C)of the molten pool can be approximately through $C = \pi \cdot (L_I + L_S)/2$. Fig. 6d shows the temperature profile and cooling rate versus time at the top of the quasi-steady molten pool where X = 3.875 mm. The temperature rise rate of metal liquid is higher than that of cooling rate, which is consistent with the phenomenon that the G at the front end of the molten pool is greater than that at the end. The liquid lifetime is 339 ms. Therefore, the effective movement distance and recycling times of metal liquid within the molten pool are 24.08 mm and 6.67 times respectively. This phenomenon led to the sufficient diffusion of solute atoms such as Fe, Cr, Ni, B, Nb within the molten pool.

4.2. Phases analysis

The phase of the material is an important indicator that determines its microstructure and mechanical properties [28,29]. As seen in Fig. 7, the X-ray diffraction(XRD) results show that the composite powder contains [Fe-Cr] solid solution, pure Nb, and B_4C powders. After the composite powders were irradiated by laser and solidified rapidly, four peaks in the diffraction spectra at 34.95° , 41.68° , 58.38° , 69.63° can be assigned to NbC with different lattice in the composite coating. Besides, the composite coating also contains [Fe-Cr] solid solution, Fe₂B, FeC, B_4C , and extremely few pure Nb. This indicates that the NbC in the

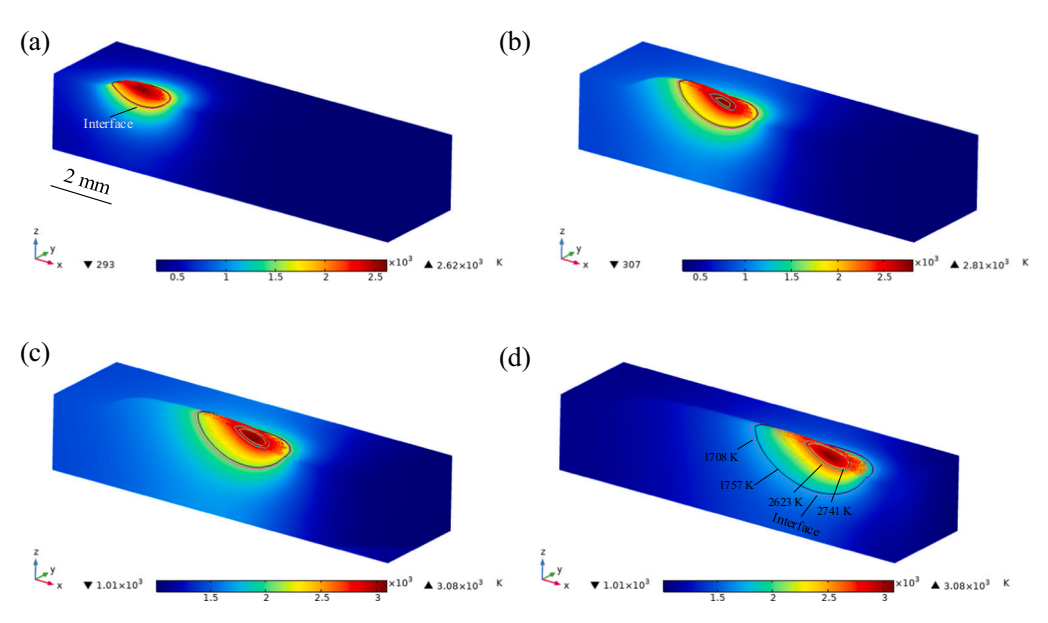


Fig. 5. The temperature evolution of composite coating; (a) 100 ms, (b) 300 ms, (c) 500 ms, (d) 750 ms.

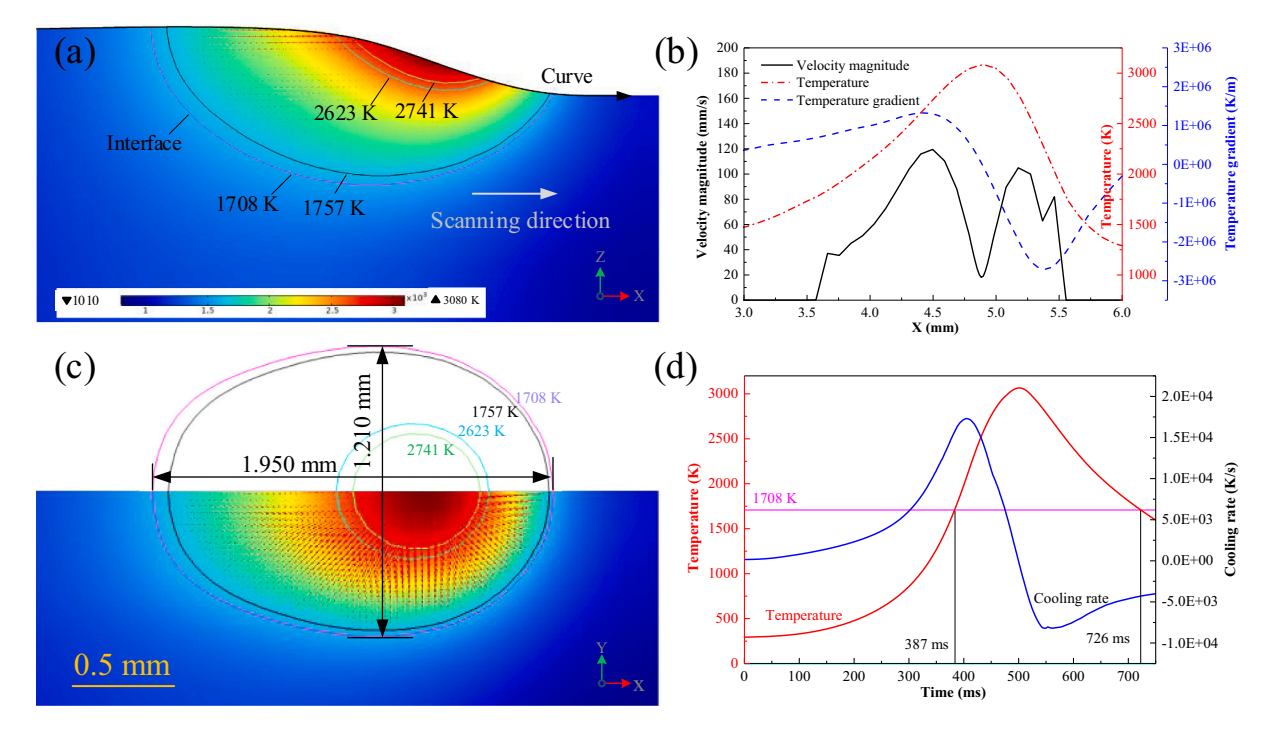


Fig. 6. The superimposed temperature and velocity fields of the quasi-steady molten pool. (a) Side view, (b) velocity, temperature and temperature gradient distribution on surface of molten pool, (c) top view, (d) the temperature profile and cooling rate at the top of molten pool where X = 3.875 mm.

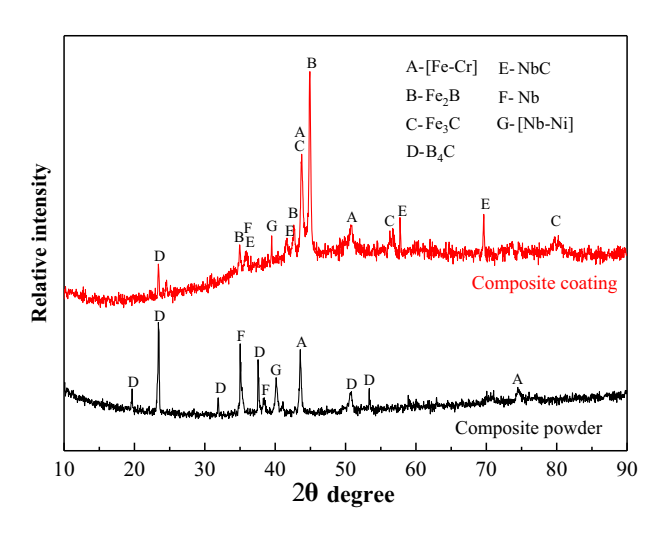


Fig. 7. XRD results from the composite powder and the composite coating.

composite coating is in-situ synthesized. To better reveal the mechanism of the in-situ reaction, the temperature-dependent Gibbs free energy $(\Delta G_{\rm T}^{\theta})$ of potential reactions were obtained, as shown in Fig. 8. According to the laws of thermodynamics, the direction and order of the chemical reaction can be judged by $\Delta G_{\rm T}^{\theta}$ [30]. It can be seen from the $\Delta G_{\rm T}^{\theta}$ – T curves when the temperature (T) >0, $\Delta G_T^{\theta}[reations2^{\#} \text{ and } 8^{\#}] < 0$. This indicates that NbC can be in-situ synthesized by reaction reactions 2# and $8^{\#}$ when T>0. Note that the lager $|\Delta G_{T}^{\theta}[\text{reaction}\mathbf{2}^{\#}\text{and }8^{\#}]|$ indicates their better thermodynamic stability. The occurrence of reaction $2^{\#}$ promoted the precipitation of element B. The B can combine Cr and rich Fe to form CrB, Fe₂B and FeB, and the reaction order is as follows: $5^{\#} > 4^{\#} > 3^{\#}$ without considering the concentration of elements. Fig. 8 shows that the highest diffraction peak in the composite coating corresponds to Fe₂B, and no CrB and FeB are found in composite coating. The low concentration of Cr and relatively small $|\Delta G_T^{\theta}[\text{reaction}3^{\#}]|$ might limit the reactions $5^{\#}$ and $3^{\#}$. Similar results also were observed in

previous studies [31,32]. The dissolution of B₄C increased the content of graphite in the molten pool when the T>2605 K according to $\Delta G_T^{\theta}[{\rm reaction1}^{\#}]$. The C can spontaneously react with Cr, Fe, and Nb elements to form Cr₃C₂, Fe₃C, and NbC due to $\Delta G_T^{\theta}[{\rm reaction6}^{\#}-8]^{\#}<0$. Moreover, the expected $|\Delta G_T^{\theta}[{\rm reaction8}^{\#}]|$ is the biggest, which indicates that the C can preferentially react with the Nb to form the NbC instead of Cr₃C₂ and Fe₃C.

To identify the different phases distinctly in the composite coating, the EDS was carried out. The results are shown in Fig. 9 and Table 4. From Fig. 9, the phase composition of the composite coating consisted of large petaloid and small round white particles (S1-S3), striped precipitated phases (S4), and the matrix (S5). From Table 4, the white particles (S1 and S2) are mainly composed of Nb and C elements, and the atomic ratio of Nb to C is close to 1 without considering the measurement error of the light elements (such as B and C) content by the SEM. The shape and color of the particles (S1 and S2) are similar to previous studies on NbC [33,34]. Combined with XRD results in Fig. 7, the white particles can be identified as in suit formed NbC particles. It is worth noting that the content of the C element in the center of small round particles (S3) is significantly higher than that of large polygonal particles (S1 and S2). Since the B₄C particles can react with rich Fe in the composite coating to form the borides, this phenomenon increases the content of graphite in the coating. Since the $\Delta G_{\mathbf{T}}^{\theta}$ [reaction8[#]] is lowest in Fig. 8, the graphite preferably reacts with the surrounding Nb atoms to form NbC particles. However, the C has no enough time to diffuse and react with metal atoms completely due to small size of the formed NbC particles, which leads to a large number of C atoms remaining in the center of small NbC particles. Since carbides, borides, [Fe, Cr] solid solution have been confirmed in XRD analysis of composite coating, the striped precipitated phases (S4) primarily contain Fe, B, Cr, and C elements, which might correspond Fe₂B, Fe₃C and [Fe, Cr] solid solution. When striped precipitated phases (carbides and borides) completely precipitated from the liquid phases, the rich metallic liquid in Fe and Ni elements solidified to form the matrix (S5), which could be used to support the strengthening phases.

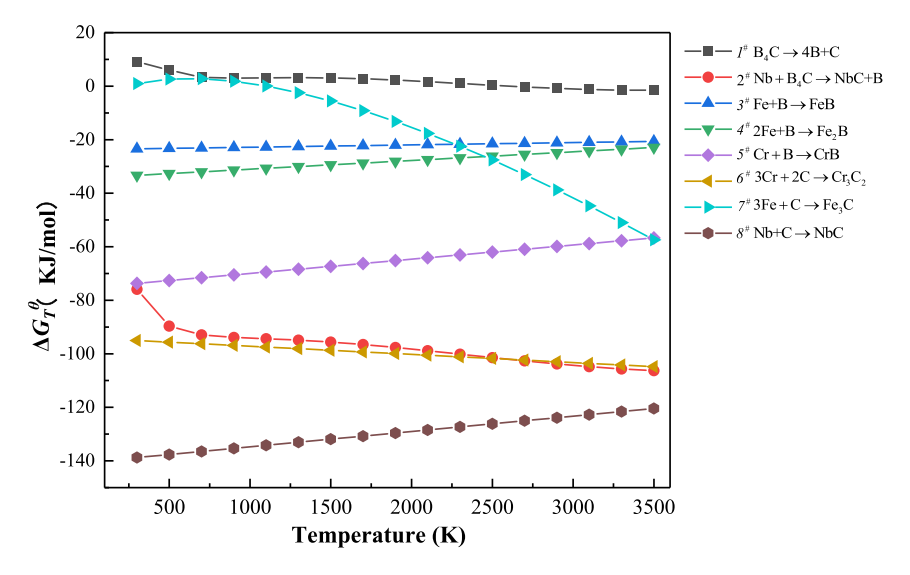


Fig. 8. The temperature-dependent Gibbs free energy for potential reactions.

4.3. Solidification characteristics

Fig. 10 shows experimental and computed cross-section morphologies of the composite coating. The cladding angle (θ) is the most commonly used factor to evaluate whether the coating alloy can form a strong metallurgical bond with the substrate, and can be expressed by θ = $(\theta_1 + \theta_2)/2$ [35]. Table 5 shows that the experiment and computed results are well-matched, and the relative error is less than 12.0%. This verifies the 3D Multiphysics model in simulating the laser cladding process. Fig. 10 also shows that the composite coating has no cracks in the inner or surface, a low dilution ratio, and a large cladding angle, which are helpful for the preparation of multi-track coatings for industrial applications. It should be noted that there are some pores on the upper surface. The porosity was mainly caused by gases (such as CO₂ or CO generated between B₄C and O₂) that don't have time to escape from the molten pool during the solidification process [36]. The porosity can be reduced by increasing the shielding gas rate or in a vacuum during laser cladding [16,37].

Temperature gradient (G) and solidification rate (R) of the solidification front are the two main parameters that affect the solidified microstructure [25,38]. The G and R ahead of the solidification front are described as Eqs. (13) and (14) [39].

$$G = \sqrt{\left(\frac{\partial T}{\partial x}\right)^2 + \left(\frac{\partial T}{\partial y}\right)^2 + \left(\frac{\partial T}{\partial z}\right)^2}$$
 (13)

$$R = V_s \cdot \cos\theta \tag{14}$$

where V_s is scanning speed, θ is the angle between R and V_s , as shown in Fig. 11. The coordinates of the solidification front (liquidus isotherm) in the X-Z plane was firstly extracted, and then the angle θ could be obtained by differentiating the coordinates of the solidification front. Since the microstructure highly depends on the thermal parameters at the solidification front, the thermal parameters extracted in this study can better reveal the solidification process than those within molten pool in previous studies [20,40,41]. Fig. 11 shows that R of the solidification front gradually decreases along the X-axis, while the G increases rapidly due to the good heat dissipation at the bottom of the molten pool [42].

Gäumann et al. [40] proposed a widely accepted thermodynamics and kinetics model for the columnar to equiaxed transformation (CET), as formulated in Eq. (15)

$$\frac{G^n}{R} = \mathbf{a} \left\{ \left(\frac{-4\pi N_0}{3\ln(1-\varphi)} \right) \cdot \frac{1}{\mathbf{n}+1} \right\}^{\mathbf{n}}$$
 (15)

where **n** and **a** are the alloy constants, which are assumed in this paper are 1.25×10^6 and 3.4 [40,42,43], the φ is the volume fraction of equiaxed or stray grains, N_0 is the nucleation density that mainly depends on the solute concentration and undercooling, and can be defined by [43].

$$N_0 = \int_0^{\Delta T} \frac{\Delta N \cdot I_0}{GV} exp\left(\frac{-\Delta G_c}{R_g T}\right) d\Delta T$$
 (16)

where ΔN is the difference of heterogeneous nucleation sites and already nucleated, I_0 is constant, ΔG_c is free energy, R_g is gas constant, ΔT is the tip undercooling. In this paper, the widely accepted criterion of the equiaxed grain volume fraction (φ) was used to calculate the curve of columnar to equiaxed transition (CET) [44]. When the φ is bigger than 49.0%, the solidified microstructure effectively corresponds to fully equiaxed grains, while , the φ below 0.66% corresponds to fully columnar grains.

As seen in Fig. 12, the spatiotemporal solidification of the composite coating can be regarded as a process in which the thermal parameters of the solidification front act on the cross-section A. At the beginning of solidification (t = 500 ms), the temperature gradient is high (about 1.8 \times 10° K/m) and the solidification rate is lowest (near 0 mm/s). Extremely high G promoted the growth of grains perpendicular to the isotherm, while the lowest R increased the growth time. Therefore, the microstructure at the bottom of the composite coating is mainly columnar grains. With the shrinkage of metal liquid and the advance of solidification front, the temperature gradient decreases and the solidification rate increases rapidly. This evolution of G and R is in good agreement with previous studies on laser cladding [20,27,39]. From Fig. 12, it is evident that the microstructure is mainly columnar grains at the beginning of solidification, and columnar grains gradually decrease during the solidification process and results in a mixed region at the end of solidification.

Fig. 13 shows the different magnification SEM images at the center of solidified coatings, respectively. EDS point tests in partially enlarged view are shown in Table 6. Since the S6 and S7 are rich in Fe and Cr in Fig. 13(b), the equiaxed grains could be identified as γ -[Fe—Cr] solid solution combining with XRD results. EDS results also show the white particles, striped phases, and matrix are identified to be the in-situ formed NbC, borides and [Fe-Cr] solid solution, respectively. The microstructure of Fe-based coating is a typical equiaxed crystal, which is typical laser-clad structure [45]. When Nb and B₄C powders were added, the microstructure of the composite coating is the fine columnar grains and a network-like eutectic substance, and the grain size is significantly

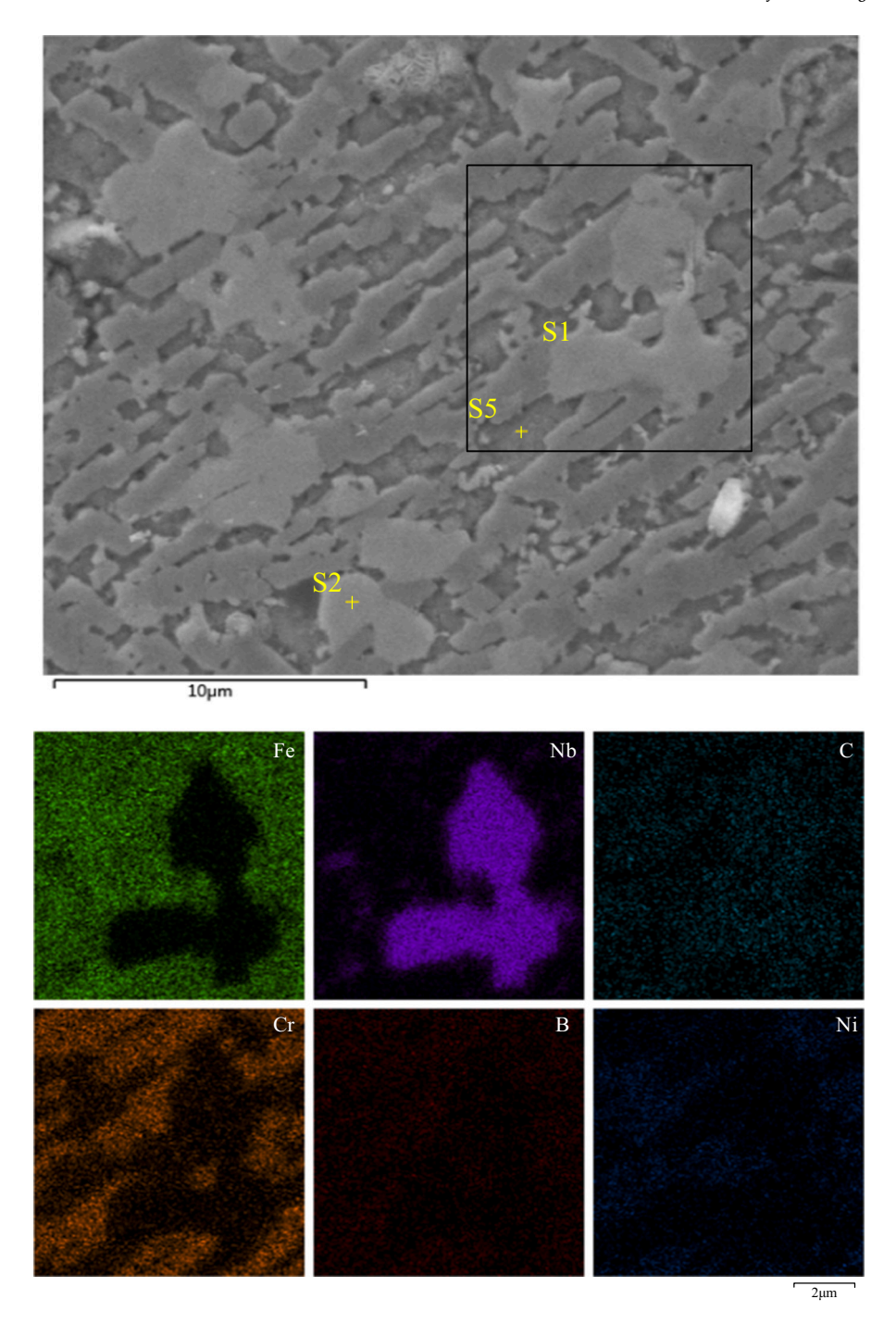


Fig. 9. EDS elemental maps of the composite coating.

Table 4 Chemical compositions of different regions marked in Fig. 9 (at. %).

Marked locations	Fe	Cr	Ni	В	Nb	С
S1	5.33	2.37	0.98	11.5	37.28	42.54
S2	0.67	1.29	1.53	19.46	35.93	41.12
S3	1.57	1.41	1.53	11.05	13.45	70.99
S4	49.94	8.05	1.78	28.73	0.92	2.58
S5	67.03	9.65	11.09	6.24	4.55	1.44

reduced. The experimental result can be consistent with the simulation tendency, as shown in Fig. 12. Moreover, the number of grains in the composite coating was larger than that in the Fe-based coating, which indicates that the addition of Nb and B_4C particles increased the

nucleation rate. The phenomenon of reducing the grain size is called as fine-grained strengthening, which can improve the mechanical properties (such as toughness and hardness) of the coating. From Fig. 13(c), the large petaloid and small round white ceramics particles are evenly distributed, and its average diameter (1.03 μm) is smaller than that (5.58 μm) of the equiaxed grains in the Fe-based coating. In-suit formed ceramics particles can increase the resistance of deformation, and the difficulty of grain sliding, thus can improve the strength and hardness of the coating. Therefore, in-situ formed fine NbC particles at the grain boundary can achieve dispersion strengthening effect on the coating.

Based on the simulation results, microstructure, and phases analysis, the phases evolution and the strengthening mechanism in two kinds of coatings can be explained as follow. Fig. 14. presents the evolution of

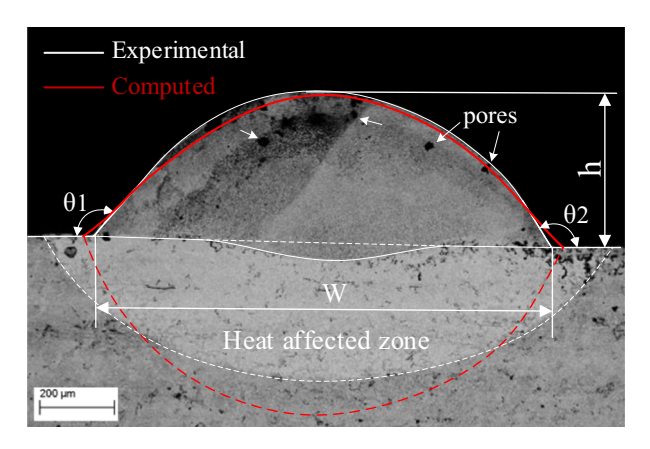


Fig. 10. Experimental and computed cross-sections of the composite coating.

Table 5Experimental and computed results of the composite coating.

	Experimental	Simulated	Absolute error	Relative error
Width (h)	1152 μm	1210 μm	58 μm	5.03%
High (W)	368 µm	340 µm	28 μm	7.61%
Cladding angle	124.6°	139.0°	14.4°	11.56%
(θ)				

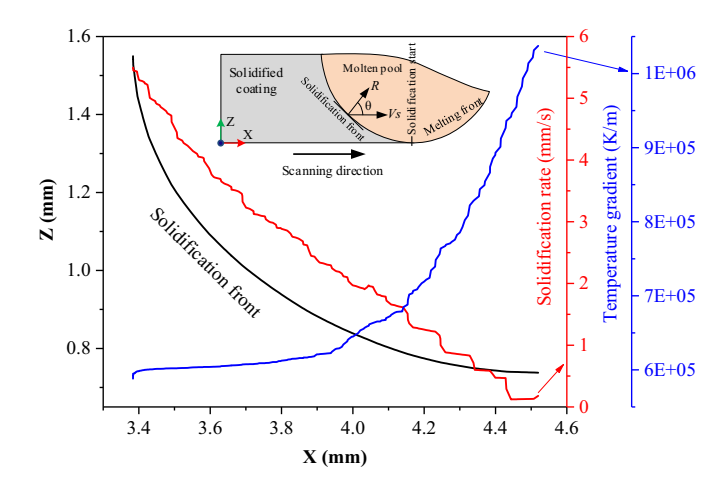


Fig. 11. Computed the G and R of the solidification front.

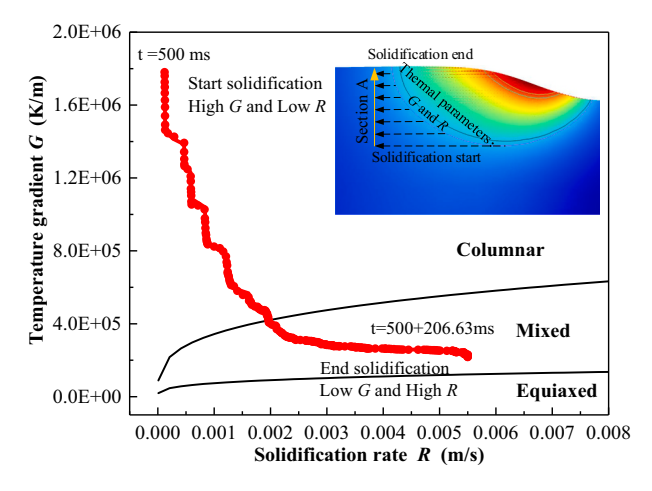


Fig. 12. Solidification process of composite coating.

microstructure and phases. As shown in Fig. 14a, at the beginning of solidification of Fe-based coating, solute atoms Fe and Cr were separated from the alloy liquid, and some local nucleation points were formed. The uniform diffusion of solute atoms and the stable derivation of interfacial crystallization latent heat promoted the stable growth of grains. Finally, the equiaxed grains were formed, as shown in Fig. 13a. As can be seen in Fig. 14c, the solute atoms were evenly distributed due to Marangoni convection. At the beginning of solidification of composite coating, since the melting point of NbC (3500 K) is greater than that of the Fe₂B, Fe₃C, and Cr₃C₂ [22], NbC precipitated out from the alloy liquid firstly owning to its lowest Gibbs free energy (Fig. 8). The crystal lattice of NbC is a typical face-centered cubic structure, corresponding preferential growth surface is (111) lattice orientation [46]. Therefore, the NbC ceramics were prone to form large octahedron structures, as seen in Fig. 13(c). The small round NbC particles in the composite coating may be due to insufficient growth. With the growth of NbC ceramics, the solute atoms such as Fe, Cr, Ni, and B in the alloy liquid were squeezed to the interface between NbC and alloy liquid. With the further solidification of alloy liquid, the enrichment of Fe and B atoms increased the nucleation sites for Fe₂B. Therefore, the nucleation rate was increased finally, which can be verified by comparing the number of grains in Fig. 13(a) and (c). Then, the growth of Fe₂B is inhibited by formed the uniformity NbC particles, which leads to the formation of long striped and irregular oriented Fe₂B. These grain structures are completely different from that of typical laser-clad coating [45]. The behavior of the precipitated NbC ceramics to refine the microstructure and grains can be called pinning effect. With the temperature decreasing continuously, the remaining solute atoms such as Fe, Cr, and Ni, are further precipitated to form the matrix ([Fe-Cr-Ni] solid solution), and the phases of solidified composite coating completely are shown in Fig. 14(d).

4.4. Mechanical properties

4.4.1. Hardness test

Fig. 15 shows the hardness and hardness indentation morphology of the coating. The average hardness of the substrate, heat-affected zone (HAZ) and the composite coating are 219.43, 628.13 and 866.36 $HV_{0.5}$, respectively. The hardness of the Fe-based coating without adding Nb and B_4C particles is 225.00 HV_{0.5}. The hardness of the composite coating is 3.95 times and 4.16 times that of the substrate and Fe-based coatings, respectively. This indicates the hardness of the Fe-based coating is greatly improved due to the addition of Nb and B₄C particles. Fig. 15(a) shows that the size of the indentation on the composite coating is significantly reduced compared with that on the substrate. As seen in Fig. 15(b), the fine in-suit NbC (hardness 24.1 GPa) and Fe₂B in the composite coating are uniformly distributed near the hardness indentation, which is beneficial to increase the deformation resistance of the composite coating. This is mainly due to the contribution of two aspects. On the one hand, the in-suit formed hard phases is indeed sufficient to increase the hardness according to many kinds of literature [47,48]. On the other hand, the fine-grained strengthening on coating also can improve the deformability by refining the microstructure (see Fig. 13). It is worth noting that the hardness of the composite coating is much higher than that of previous studies on NbC-reinforced coatings [9,49,50]. This may be due to the rich and high-hardness Fe₂B (19.0 GPa) phases generated by the addition of B₄C particles. One also can be found that the hardness of the HAZ is 2.86 times that of the substrate. Since the substrate is a Fe-based material with a carbon content of 0.45%, the high-speed cooling rate of the material in the HAZ will cause the transformation from α – Fe to martensite [51,52], which can significantly increase the hardness in the HAZ.

4.4.2. Wear performance

Since wear is an important factor leading to the failure of mechanical parts under severe conditions, it is of great significance to study the mechanism of reinforced phases to improve the wear resistance. Fig. 16

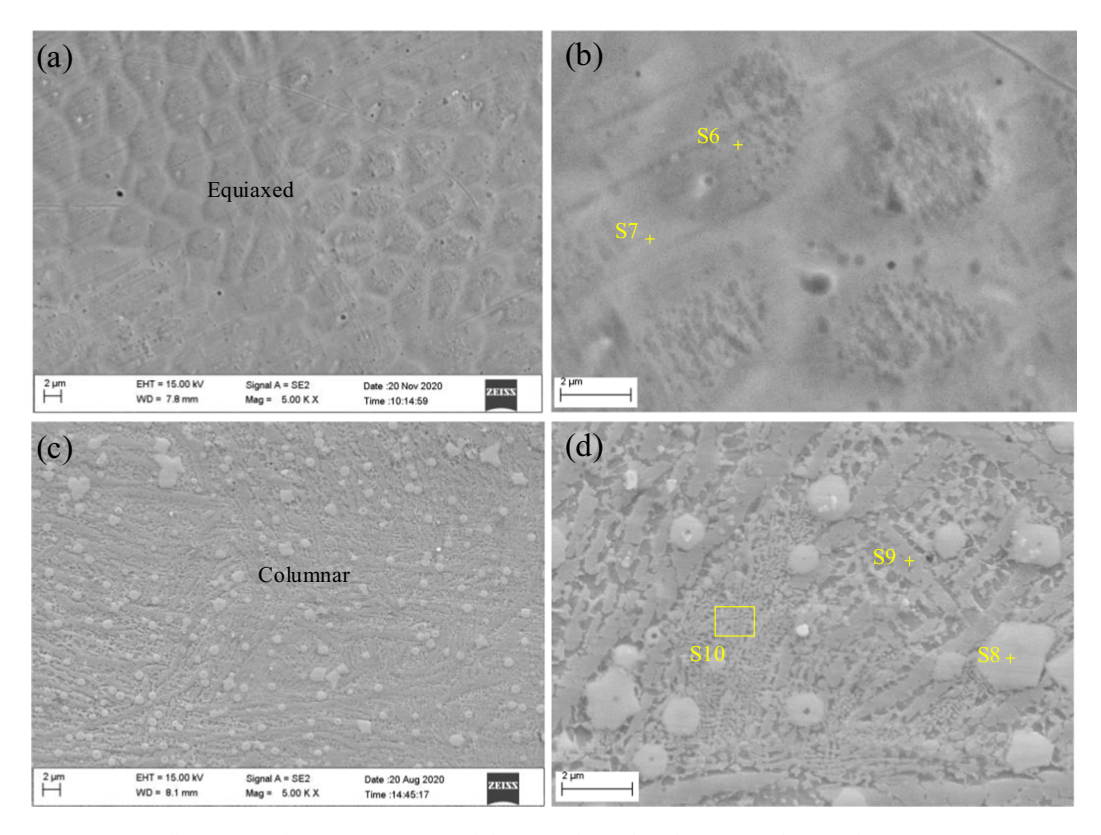


Fig. 13. Different magnification SEM images of the (a) & (b): Fe-based coating and (c) & (d): composite coating.

Table 6
EDS tests results in Fig. 13 (at. %).

Marked locations	Fe	Cr	Si	Ni	В	Mn	Nb	С
S6	73.71	14.23	1.05	8.34	_	1.45	_	0.29
S7	68.22	16.49	1.80	9.49	-	1.97	-	0.33
S8	5.33	2.37	_	0.98	0.59	_	48.18	42.54
S9	56.12	7.08	1.16	4.26	27.07	0.91	1.27	2.13
S10	80.99	4.96	1.30	8.43	-	1.04	1.54	1.73

shows the friction coefficient vs the sliding time. The friction coefficient is unstable at the beginning of the sliding, but it tends to a stable value after 25 minters. The average friction coefficient of the composite coating is 0.405, which is 0.775 times of the Fe-based coating and 0.879 times of the substrate. Moreover, the wear curve of composite coatings is more stable than that of the Fe-based coating and substrate. Fig. 17 shows the typical 3D morphology and 2D cross-section profile of wear track. It shows that the weak track of Fe-based coating is the widest, while that of composite coating is the narrowest. This can indirectly reflect the good wear resistance of the composite coating. To observe the wear morphology in detail and calculate the wear volume, the 2D crosssection profiles of the wear track on sections S1, S2 and S3 were extracted, as shown in Fig. 17(d). The wear volume was calculated based on Eq. (10). The volume loss for the composite coating (6.28×10^{-3}) mm³) was 0.167 times that for substrate (37.54 \times 10⁻³ mm³) and 0.175 times that for Fe-based coating (35.97 $10^{-3} \times \text{mm}^3$). The wear tracks on the substrate and Fe-based coating show its lager deformation and deeper grooves, which corresponds to larger wear removal. The volume bulge at the edge of the wear track for substrate and Fe-based coating can also be observed, which may be caused by the plastic deformation of the material during wear process. After adding Nb and B₄C powders, the 2D cross-section profiles for composite coating is the smoothest among the three wear tracks. The large grooves on the worn surface are eliminated. This phenomenon improves the smoothness of the friction curve.

To reveal the wear mechanism of the coating in detail, the 2D and 3D

worn surface morphologies of each coating was observed, as shown in Fig. 18. As illustrated in Fig. 18(a), there is a deep groove along the sliding direction on the worn surface of substrate, indicating the occurrence of abrasive wear. In the process of the high-hardness friction pair (HRC > 90) sliding against the low hardness substrate (α – Fe, about 200 HV_{0.5}), the large plastic deformation of the substrate led to the rapid removal of the material, and form abrasive particles. As the slide continues, the abrasive particles micro-cut the substrate, and finally a large groove is formed on the worn surface. Due to the rapid cooling during laser cladding, there would be thermal effects and residual stresses in the coating [53,54]. The high and concentrated stress would promote the propagation of micro-cracks, so the flakes or scaly flakes are precipitated from the worn surface, as shown in Fig. 18(b). This phenomenon leads to significantly more spalling on the Fe-based coatings than on the substrate. Therefore, it can be found that the wear properties of the substrate and Fe-based coating is poor. The microstructure (Fig. 13c) and worn surface (Fig. 18c) of the composite coating show that in-situ NbC and Fe₂B, and unmelted B₄C particles are evenly distributed. It is worth noting that fine structure with long striped and irregular oriented size (Fig. 13c) can not only improve the wear resistance [55] but also increase the toughness of the matrix, thus improving the holding force of hard particles. Therefore, the hard phases used to bear heavy load are difficult to peel off from the matrix. Since the hard phases bear the main load during the wear process, the material on the surface of the matrix ([Fe-Cr] solid solution, about 250.0 HV_{0.5}) is

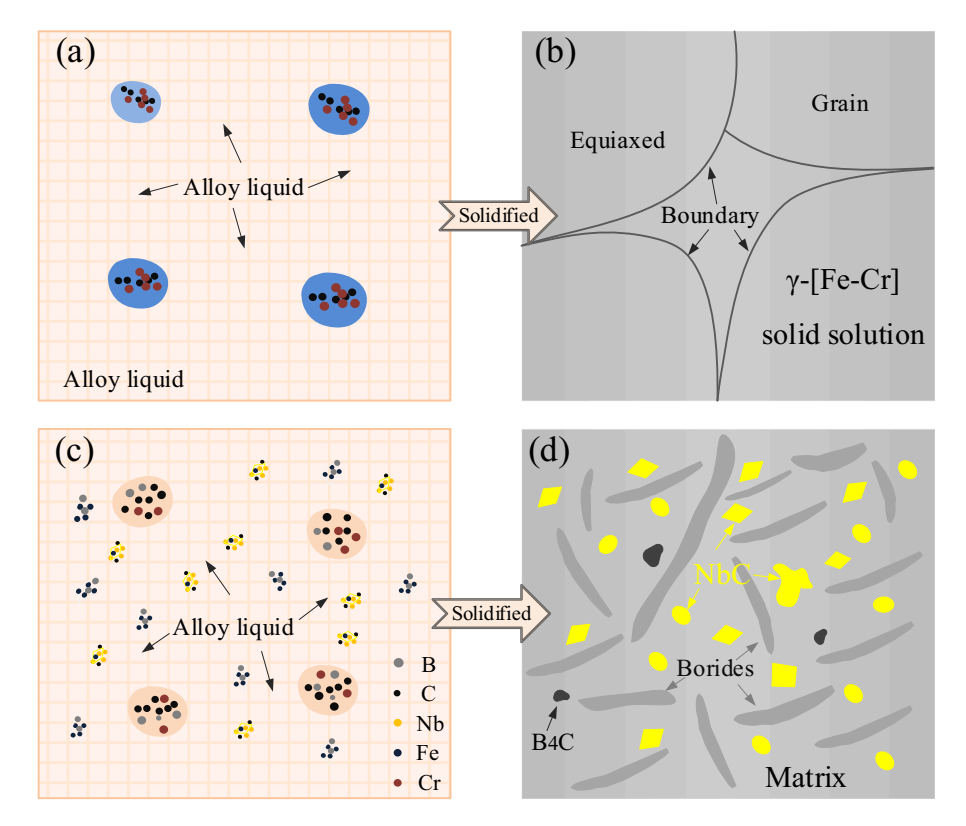


Fig. 14. The microstructure and phases evolution of the (a) & (b): Fe-based coating and (c) & (d): composite coating.

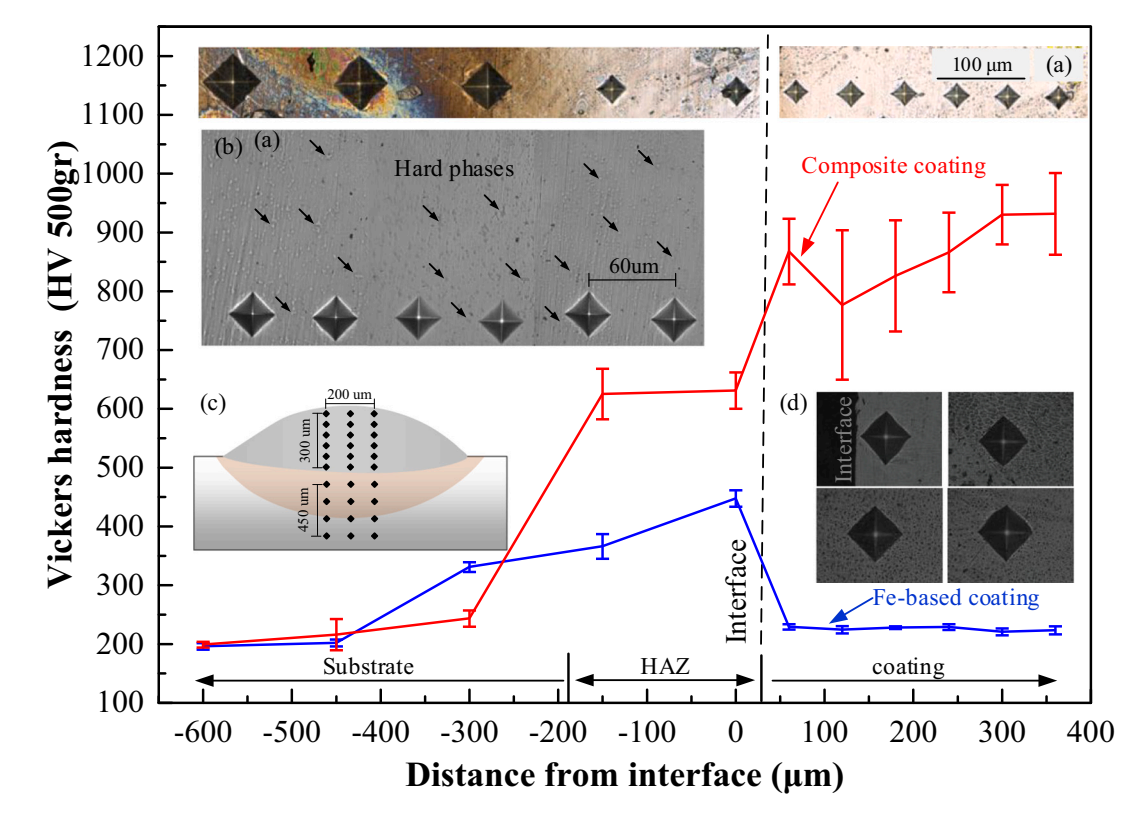


Fig. 15. Hardness and hardness indentation morphology. (a) and (b): composite coting, (c): indentation distribution diagram, (d): Fe-based coating.

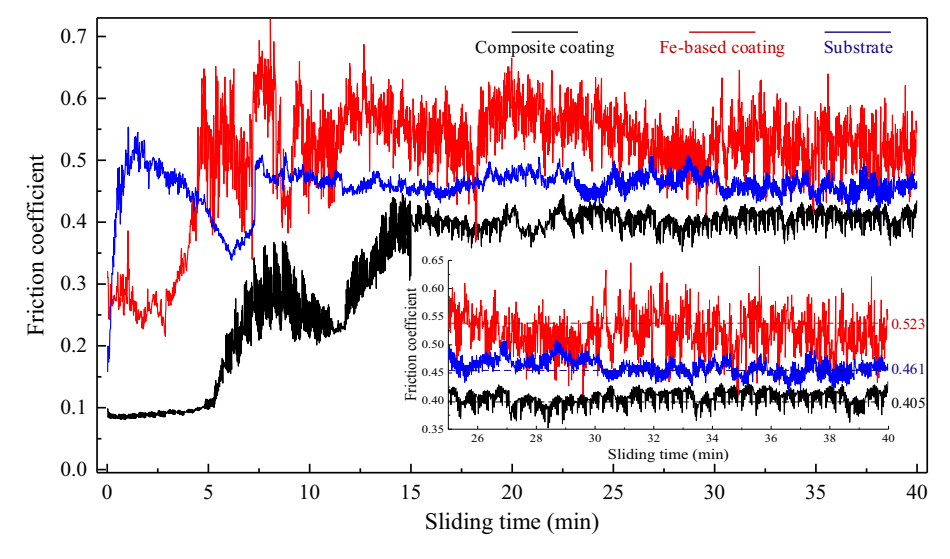


Fig. 16. The friction coefficient of the substrate, Fe-based coating and composite coating.

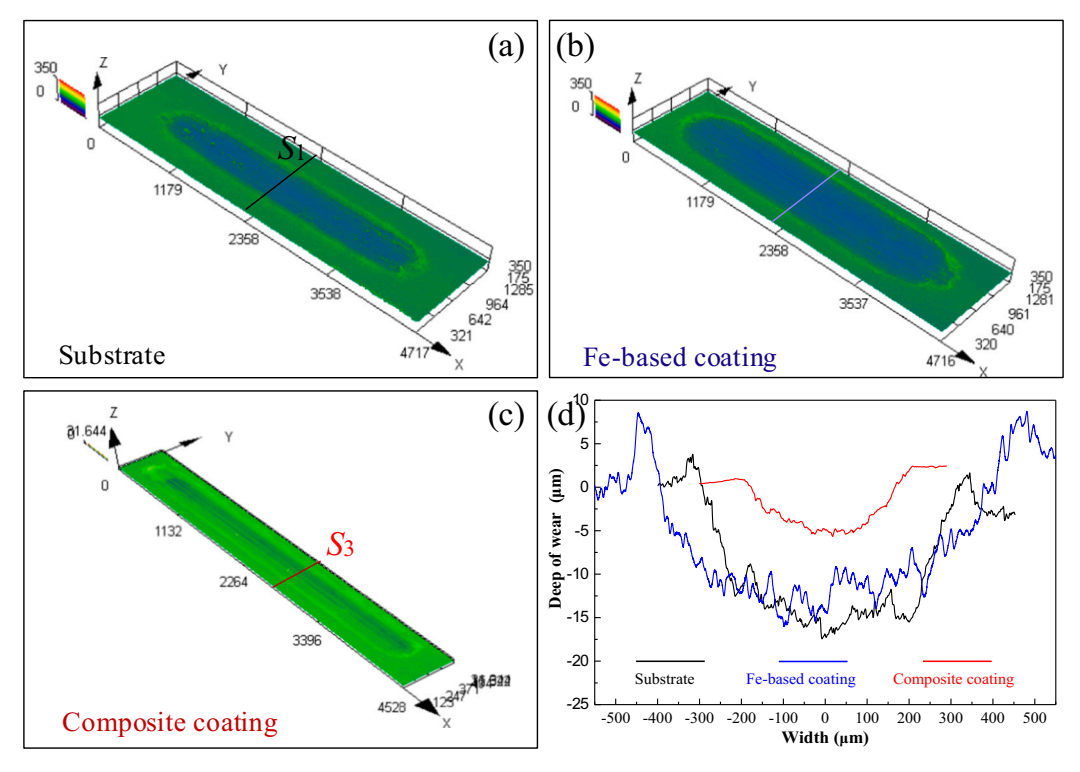


Fig. 17. The 3D wear morphology of the (a) substrate, (b) Fe-based coating, and (c) composite coating; (d) 2D profles of wear tracks.

not easily removed by the friction pair during the sliding process. This can reduce the wear rate of the composite coating. In the process of repeated friction, some abrasive debris peeled off due to fatigue wear are pressed on the friction pair and play a lubrication role to some extent. The worn form gradually changes to adhesive wear after repeated sliding, so the worn surface is smoother as shown in Fig. 18(c).

5. Conclusions

In this study, in-situ formed NbC and Fe $_2$ B reinforced Fe-based composite coating was applied to the surface modification of medium carbon steel. The temperature conditions and mechanism of in-situ reaction were revealed in detail by thermodynamic calculation and the Multi-physical field model, which can provide theoretical guidance for

improving the mechanical properties of MMC coating. The main results of this study can be summarized as follows:

- 1. The simulated temperature field shows that the maximum temperature within the molten pool is more than 3000 K. Combined with thermodynamic calculation, in-situ formation of NbC can be carried out by the reaction between B_4C and Nb. The simulated velocity field shows that the effective movement distance and recycling times of alloy liquid are 24.08 mm and 6.67 times due to Marangoni convection. This mass transfer behavior not only promoted the melting of particles with high-melting point but also improved the uniformity of solute atoms.
- 2. The main phases in Fe-based coating were [Fe-Cr] solid solution. With Nb and B_4C addition, the formation of [Fe-Cr] solid solution

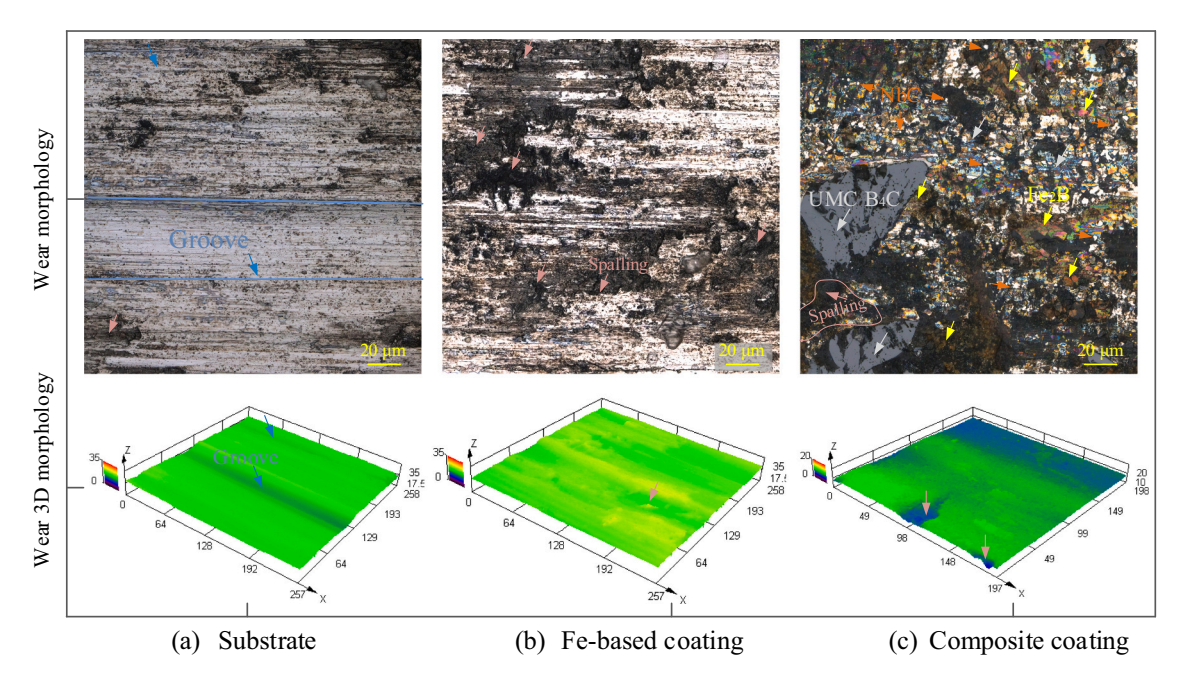


Fig. 18. Worn surface of the substrate, Fe-based coating, and composite coating.

was suppressed, and uniformly distributed NbC and Fe₂B were in-situ synthesized. The formation of NbC phase was attributed to its lowest $\Delta G_{\rm T}^{\theta}$, while the formation of Fe₂B was attributed to the rich iron and boron atoms.

- 3. The microstructure in original Fe-based coating was typical laser-clad equiaxed grains, while the microstructure in composite coating was columnar grains with long striped and irregular oriented shape, which was consistent with the simulation tendency (CET model). The in-situ NbC (average diameter $\sim 1.03~\mu m$) achieved the fine-grained strengthening of the coating by its pinning effect.
- 4. The hardness of the composite coating is $866.36~HV_{0.5}$, which is 3.95~times and 4.16~times that of the substrate and Fe-based coatings, respectively. The in-situ formed NbC, grain refinement, and rich formed Fe₂B are helpful to improve the hardness of the coating.
- 5. The average friction coefficient of the composite coating is 0.405, which is 0.775 times of the Fe-based coating and 0.879 times of the substrate. The wear mechanism of the coating changed from abrasive wear to adhesive wear due to the addition of Nb and B_4C powders.

Declaration of competing interest

No conflict of interest exists in the submission of this manuscript, and the manuscript is approved by all authors for publication. I would like to declare on behalf of my co-authors that the work described was original research that has not been published previously, and not under consideration for publication elsewhere, in whole or in part. The authors declare that they have no known competing financial interests or personal relationships that could have appeared to influence the work reported in this paper.

Acknowledgment

This work was support by the Fundamental Research Funds for the Central Universities (N2003026); the National Natural Science Foundation of China (52075088).

References

[1] L. Song, G. Zeng, H. Xiao, X. Xiao, S. Li, Repair of 304 stainless steel by laser cladding with 316L stainless steel powders followed by laser surface alloying with

- WC powders, J. Manuf. Process. 24 (2016) 116–124. https://linkinghub.elsevier.com/retrieve/pii/\$1526612516300986
- [2] G.F. Sun, X.T. Shen, Z.D. Wang, M.J. Zhan, S. Yao, R. Zhou, Z.H. Ni, Laser metal deposition as repair technology for 316L stainless steel: influence of feeding powder compositions on microstructure and mechanical properties, Opt. Laser Technol. 109 (2019) 71–83. https://linkinghub.elsevier.com/retrieve/pii /S0030399218302032.
- [3] W. Gao, S. Zhao, Y. Wang, F. Liu, C. Zhou, X. Lin, Effect of re-melting on the cladding coating of Fe-based composite powder, Mater. Des. 64 (2014) 490–496. https://linkinghub.elsevier.com/retrieve/pii/S0261306914006098.
- [4] M. Qunshuang, L. Yajiang, W. Juan, Effects of Ti addition on microstructure homogenization and wear resistance of wide-band laser clad Ni60/WC composite coatings, Int. J. Refract. Met. Hard Mater. 64 (2017) 225–233. https://linkinghub. elsevier.com/retrieve/pii/S026343681630525X.
- [5] J. Meng, X. Shi, S. Zhang, M. Wang, F. Xue, B. Liu, W. Cui, L. Bian, Friction and wear properties of TiN-TiB2-Ni based composite coatings by argon arc cladding technology, Surf. Coat. Technol. 374 (2019) 437–447. https://linkinghub.elsevier. com/retrieve/pii/S0257897219306292.
- [6] N. Ma, J. Chen, Z. Huang, X. Liu, Z. Chen, Densification of C/SiC composite surface by the hybrid process of laser cladding and subsequent heat treatment, Ceram. Int. 45 (2019) 7703–7708. https://linkinghub.elsevier.com/retrieve/pii/S0272884 219300768. https://api.elsevier.com/content/article/PII:S0272884219300768? httpAccept=text/xml.
- [7] Y. Hu, W. Cong, A review on laser deposition-additive manufacturing of ceramics and ceramic reinforced metal matrix composites, Ceram. Int. 44 (2018) 20599–20612. https://linkinghub.elsevier.com/retrieve/pii/S02728842183214 12.
- [8] K.H. Lo, F.T. Cheng, C.T. Kwok, H.C. Man, Improvement of cavitation erosion resistance of AISI 316 stainless steel by laser surface alloying using fine WC powder, Surf. Coat. Technol. 165 (2003) 258–267. https://www.sciencedirect.com/science/article/pii/S0257897202007399.
- [9] Y. Cao, S. Zhi, H. Qi, Y. Zhang, C. Qin, S. Yang, Evolution behavior of ex-situ NbC and properties of Fe-based laser clad coating, Opt. Laser Technol. 124 (2020), 105999. https://linkinghub.elsevier.com/retrieve/pii/S0030399218315627.
- [10] C.L. Wu, S. Zhang, C.H. Zhang, J.B. Zhang, Y. Liu, J. Chen, Effects of SiC content on phase evolution and corrosion behavior of SiC-reinforced 316L stainless steel matrix composites by laser melting deposition, Opt. Laser Technol. 115 (2019) 134–139. https://linkinghub.elsevier.com/retrieve/pii/S0030399217318443.
- [11] H. Zeinali Moghaddam, M. Sharifitabar, G. Roudini, Microstructure and wear properties of Fe–TiC composite coatings produced by submerged arc cladding process using ferroalloy powder mixtures, Surf. Coat. Technol. 361 (2019) 91–101. https://linkinghub.elsevier.com/retrieve/pii/S0257897219300623.
- [12] C. Cui, Z. Guo, H. Wang, J. Hu, In situ TiC particles reinforced grey cast iron composite fabricated by laser cladding of Ni-Ti-C system, J. Mater. Process. Technol. 183 (2007) 380–385, https://doi.org/10.1016/j.jmatprotec.2006.10.031.
- [13] X. Zeng, T. Yamaguchi, K. Nishio, Characteristics of Ti(C, N)/TiB composite layer on Ti-6Al-4V alloy produced by laser surface melting, Opt. Laser Technol. 80 (2016) 84–91, https://doi.org/10.1016/j.optlastec.2016.01.004.
- [14] B. AlMangour, D. Grzesiak, J.M. Yang, In-situ formation of novel TiC-particle-reinforced 316L stainless steel bulk-form composites by selective laser melting, J. Alloys Compd. 706 (2017) 409–418, https://doi.org/10.1016/j.jallcom.2017.01.149.

- [15] D. Tijo, M. Masanta, A.K. Das, In-situ TiC-TiB2 coating on Ti-6Al-4V alloy by tungsten inert gas (TIG) cladding method: part-I. Microstructure evolution, Surf. Coat. Technol. 344 (2018) 541–552, https://doi.org/10.1016/j. surfcoat 2018 03 082
- [16] S. Sun, H. Fu, X. Ping, X. Guo, J. Lin, Y. Lei, W. Wu, J. Zhou, Effect of CeO2 addition on microstructure and mechanical properties of in-situ (Ti, Nb)C/Ni coating, Surf. Coat. Technol. 359 (2019) 300–313. https://linkinghub.elsevier.com/retrieve/pii/S0257897218314087.
- [17] X. Pang, F. Zhou, Thermostability and weatherability of TiN/TiC-Ni/Mo solar absorption coating by spray method-laser cladding hybrid deposition, Opt. Lasers Eng. 127 (2020), 105983. https://linkinghub.elsevier.com/retrieve/pii /S0143816619312291.
- [18] X.H. Wang, S.L. Song, S.Y. Qu, Z.D. Zou, Characterization of in situ synthesized TiC particle reinforced Fe-based composite coatings produced by multi-pass overlapping GTAW melting process, Surf. Coat. Technol. 201 (2007) 5899–5905, https://doi.org/10.1016/j.surfcoat.2006.10.042.
- [19] X. Wang, X. Pan, B. Du, S. Li, Production of in situ TiB2+TiC/Fe composite coating from precursor containing B4C-TiO2-Al powders by laser cladding, Trans. Nonferrous Metals Soc. China 23 (2013) 1689–1693. https://linkinghub.elsevier. com/retrieve/pii/S1003632613626497.
- [20] A.K. Mishra, A. Kumar, Numerical and experimental analysis of the effect of volumetric energy absorption in powder layer on thermal-fluidic transport in selective laser melting of Ti6Al4V, Opt. Laser Technol. 111 (2019) 227–239. htt ps://linkinghub.elsevier.com/retrieve/pii/S0030399218311988.
- [21] W. Ya, B. Pathiraj, S. Liu, 2D modelling of clad geometry and resulting thermal cycles during laser cladding, J. Mater. Process. Technol. 230 (2016) 217–232. htt ps://linkinghub.elsevier.com/retrieve/pii/S0924013615301989.
- [22] C.J. Smith, C.R. Weinberger, G.B. Thompson, Phase stability and microstructural formations in the niobium carbides, J. Eur. Ceram. Soc. 38 (2018) 4850–4866, https://doi.org/10.1016/j.jeurceramsoc.2018.06.041.
- [23] J.T. W, Infrared radiation a handbook of applications, J. Mol. Struct. 7 (1971)
- [24] Y. Zhao, L. Chen, J. Sun, T. Yu, Mechanical property of YCF101 coating under different overlap modes by laser cladding, Optik (Stuttg) 212 (2020), 164714, https://doi.org/10.1016/j.ijleo.2020.164714.
- [25] N. Tamanna, R. Crouch, S. Naher, Progress in numerical simulation of the laser cladding process, Opt. Lasers Eng. 122 (2019) 151–163. https://linkinghub.else vier.com/retrieve/pii/S0143816619301149.
- [26] S. Wei, G. Wang, Y.C. Shin, Y. Rong, Comprehensive modeling of transport phenomena in laser hot-wire deposition process, Int. J. Heat Mass Transf. 125 (2018) 1356–1368. https://linkinghub.elsevier.com/retrieve/pii/S001793101 7354029.
- [27] B. Song, T. Yu, X. Jiang, W. Xi, X. Lin, The relationship between convection mechanism and solidification structure of the iron-based molten pool in metal laser direct deposition, Int. J. Mech. Sci. 165 (2020), 105207. https://linkinghub.else vier.com/retrieve/pii/S0020740319328504.
- [28] Z. Chen, H. Yan, P. Zhang, Z. Yu, Q. Lu, J. Guo, Microstructural evolution and wear behaviors of laser-clad Stellite 6/NbC/h-BN self-lubricating coatings, Surf. Coat. Technol. 372 (2019) 218–228. https://linkinghub.elsevier.com/retrieve/pii/ /S02578972113304608
- [29] H. Xiong, Z. Li, K. Zhou, TiC whisker reinforced ultra-fine TiC-based cermets: microstructure and mechanical properties, Ceram. Int. 42 (2016) 6858–6867. htt ps://linkinghub.elsevier.com/retrieve/pii/S0272884216001000.
- [30] L. Yang, T. Yu, M. Li, Y. Zhao, J. Sun, Microstructure and wear resistance of in-situ synthesized Ti(C, N) ceramic reinforced Fe-based coating by laser cladding, Ceram. Int. 44 (2018) 22538–22548. https://linkinghub.elsevier.com/retrieve/pii (20272884218234218)
- [31] A. Sudo, T. Nishi, N. Shirasu, M. Takano, M. Kurata, Fundamental experiments on phase stabilities of Fe-B-C ternary systems, J. Nucl. Sci. Technol. 52 (2015) 1308–1312, https://doi.org/10.1080/00223131.2015.1016465.
- [32] V. Homolová, L. Čiripová, A. Výrostková, Experimental study of phase composition of Fe-(30-60)B-C alloys and boron-rich corner of Fe-B-C phase diagram, J. Phase Equilib. Diffus. 36 (2015) 599–605, https://doi.org/10.1007/s11669-015-0424-0.
- [33] Y. Cao, H. Ren, C. Hu, Q. Meng, Q. Liu, In-situ formation behavior of NbC-reinforced Fe-based laser cladding coatings, Mater. Lett. 147 (2015) 61–63. htt ps://linkinghub.elsevier.com/retrieve/pii/S0167577X15002128.
- [34] J. Wang, C. Li, M. Zeng, Y. Guo, X. Feng, L. Tang, Y. Wang, Microstructural evolution and wear behaviors of NbC-reinforced Ti-based composite coating, Int. J. Adv. Manuf. Technol. 107 (2020) 2397–2407, https://doi.org/10.1007/s00170-020-05198-w.
- [35] T. Yu, L. Yang, Y. Zhao, J. Sun, B. Li, Experimental research and multi-response multi-parameter optimization of laser cladding Fe313, Opt. Laser Technol. 108

- (2018) 321–332. https://linkinghub.elsevier.com/retrieve/pii/S0030399 218304286.
- [36] Y. Zhao, T. Yu, J. Sun, S. Jiang, Microstructure and properties of laser cladded B4C/TiC/Ni-based composite coating, Int. J. Refract. Met. Hard Mater. 86 (2020), 105112. https://linkinghub.elsevier.com/retrieve/pii/S0263436819305050.
- [37] Y. Zhao, T. Yu, J. Sun, S. Jiang, Microstructure and properties of laser cladded B4C/TiC/Ni-based composite coating, Int. J. Refract. Met. Hard Mater. 86 (2020), 105112. https://linkinghub.elsevier.com/retrieve/pii/S0263436819305050.
- [38] O. Andreau, I. Koutiri, P. Peyre, J.D. Penot, N. Saintier, E. Pessard, T. De Terris, C. Dupuy, T. Baudin, Texture control of 316L parts by modulation of the melt pool morphology in selective laser melting, J. Mater. Process. Technol. 264 (2019) 21–31, https://doi.org/10.1016/j.jmatprotec.2018.08.049.
- [39] Z. Gan, G. Yu, X. He, S. Li, Numerical simulation of thermal behavior and multicomponent mass transfer in direct laser deposition of co-base alloy on steel, Int. J. Heat Mass Transf. 104 (2017) 28–38. https://linkinghub.elsevier.com/retrie ve/pii/S0017931016310377.
- [40] M. Gäumann, C. Bezençon, P. Canalis, W. Kurz, Single-crystal laser deposition of superalloys: processing-microstructure maps, Acta Mater. 49 (2001) 1051–1062, https://doi.org/10.1016/S1359-6454(00)00367-0.
- [41] Y. Liu, Z. Pang, J. Zhang, Comparative study on the influence of subsequent thermal cycling on microstructure and mechanical properties of selective laser melted 316L stainless steel, Appl. Phys. A Mater. Sci. Process. 123 (2017). http://link.springer.com/10.1007/s00339-017-1313-7.
- [42] J.M. Vitek, The effect of welding conditions on stray grain formation in single crystal welds - theoretical analysis, Acta Mater. 53 (2005) 53–67, https://doi.org/ 10.1016/j.actamat.2004.08.039.
- [43] M. Gäumann, R. Trivedi, W. Kurz, Nucleation ahead of the advancing interface in directional solidification, Mater. Sci. Eng. A 226–228 (1997) 763–769, https://doi. org/10.1016/s0921-5093(97)80081-0.
- [44] J.D. Hunt, Steady state columnar and equiaxed growth of dendrites and eutectic, Mater. Sci. Eng. 65 (1984) 75–83. http://www.sciencedirect.com/science/artic le/pii/0025541684902015.
- [45] M.J. Zhan, G.F. Sun, Z.D. Wang, X.T. Shen, Y. Yan, Z.H. Ni, Numerical and experimental investigation on laser metal deposition as repair technology for 316L stainless steel, Opt. Laser Technol. 118 (2019) 84–92, https://doi.org/10.1016/j. optlastec.2019.05.011.
- [46] Y. bin Cao, S. xin Zhi, Q. Gao, X. tao Tian, T. Geng, X. Guan, C. Qin, Formation behavior of in-situ NbC in Fe-based laser cladding coatings, Mater. Charact. 119 (2016) 159–165, https://doi.org/10.1016/j.matchar.2016.08.005.
- [47] H. Chen, Y. Lu, Y. Sun, Y. Wei, X. Wang, D. Liu, Coarse TiC particles reinforced H13 steel matrix composites produced by laser cladding, Surf. Coat. Technol. 395 (2020), 125867, https://doi.org/10.1016/j.surfcoat.2020.125867.
- [48] S. Liu, Y.C. Shin, The influences of melting degree of TiC reinforcements on microstructure and mechanical properties of laser direct deposited Ti6Al4V-TiC composites, Mater. Des. 136 (2017) 185–195. https://linkinghub.elsevier. com/retrieve/pii/S026412751730919X.
- [49] P. Xuelong, F. Hanguang, S. Shuting, L. Jian, L. Yongping, W. Wenbo, Z. Jianxin, Effect of Nb addition on microstructure and properties of laser cladding NiCrBSi coatings, Trans. Inst. Met. Finish. 96 (2018) 304–312, https://doi.org/10.1080/ 00202967 2018 1502934
- [50] Q. Li, Y. Lei, H. Fu, Laser cladding in-situ NbC particle reinforced Fe-based composite coatings with rare earth oxide addition, Surf. Coat. Technol. 239 (2014) 102–107. https://linkinghub.elsevier.com/retrieve/pii/S0257897213011183.
- [51] C. Heming, H. Xieqing, W. Honggang, Calculation of the residual stress of a 45 steel cylinder with a non-linear surface heat-transfer coefficient including phase transformation during quenching, J. Mater. Process. Technol. 89–90 (1999) 339–343, https://doi.org/10.1016/S0924-0136(99)00058-8.
- [52] S. Liu, K.M. Hong, C. Katinas, Y.C. Shin, Multiphysics modeling of phase transformation and microhardness evolution in laser direct deposited Ti6Al4V, J. Manuf. Process. 45 (2019) 579–587, https://doi.org/10.1016/j. imapro.2019.07.027.
- [53] P. Guo, B. Zou, C. Huang, H. Gao, Study on microstructure, mechanical properties and machinability of efficiently additive manufactured AISI 316L stainless steel by high-power direct laser deposition, J. Mater. Process. Technol. 240 (2017) 12–22. https://linkinghub.elsevier.com/retrieve/pii/S0924013616303181.
- [54] R.J. Moat, A.J. Pinkerton, L. Li, P.J. Withers, M. Preuss, Residual stresses in laser direct metal deposited Waspaloy, Mater. Sci. Eng. A 528 (2011) 2288–2298. htt ps://linkinghub.elsevier.com/retrieve/pii/S0921509310014036.
- [55] Y. Lin, C. Jiang, Z. Lin, Q. Chen, Y. Lei, H. Fu, Laser in-situ synthesis of high aspect ratio TiB fiber bundle reinforced titanium matrix composite coating, Opt. Laser Technol. 115 (2019) 364–373, https://doi.org/10.1016/j.optlastec.2019.02.047.